Study of fluidization transition from Geldart B to A induced by high temperature using electrical capacitance tomography

Kai Huang[1], Shuanghe Meng[1], Tao Zhang[1], W.Q. Yang[2], Mao Ye[1], and Zhongmin Liu[1]

[1]Dalian Institute of Chemical Physics, Chinese Academy of Sciences
[2]School of Electrical and Electrice Engineering

May 5, 2020

Abstract

In this paper fluidization transition from Geldart B to A induced by change in temperature was visualized by high-temperature electrical capacitance tomography (ECT) recently developed. Silica particles with a Sauter mean diameter of 222 μm and density of 2650 kg/m^3, which are typically Geldart B particles at ambient condition, were fluidized in a fluidized bed of 5 cm from 20 to 600 °C. With the increase in temperature, ECT images showed the decrease in superficial gas velocity corresponding to the onset of bubbles, i.e. the minimum bubbling velocity (U_{mb}) and homogeneous fluidization regime. The pressure drop versus superficial gas velocity curves confirmed the existence of homogeneous fluidization between the minimum fluidization velocity (U_{mf}) and U_{mb} at elevated temperature. Our detailed analysis confirms that the cohesive inter-particle forces, which manifest a linear increment with temperature, are responsible for the fluidization transition.

Introduction

Gas-solids fluidized bed reactors operated at high temperature are widely used in industrial processes, including methanol-to-olefins (MTO), fluid catalytic cracking (FCC), coal combustion, metallurgy, and polymerization, because of their good performance in heat and mass transfer.[1-7] However, it is discovered that elevated temperature could change fluidization behavior and, in severe situation, cause defluidization in fluidized beds.[1-6] For example, particle agglomeration in polymerization fluidized bed reactors induced by high temperature would lead to the reduction of fluidization quality and sometimes undesired reactor shutdown.[1-2]In a metallurgy process, cohesion between particles would be enhanced due to high temperature, which makes the particles be stuck together and difficult to be fluidized.[6] Therefore, it is very important to understand the change in fluidization behavior, especially fluidization transition in fluidized beds, induced by elevated temperature.

Geldart classified gas-solids fluidization into four different groups according to the density and size of particles.[8] In the past decades, researchers have investigated the influence of temperature on fluidization transition between different Geldart groups. Because of the lack of effective measurement techniques at high temperature, most of the previous work was carried out based on indirect measurement, e.g. pressure or pressure drop across a fluidized bed. For instance, Botterill et al.[9] studied fluidization of sand between 380 and 2320 μm up to 960°C by measuring pressure drop across a fluidized bed, and found that for small solids between 380 and 530 μm the void fraction at incipient fluidization increases with temperature. Lucas et al.[10] confirmed the increase in the minimum fluidization void fraction with elevated temperature for particles with a narrower size distribution based on pressure drop across a fluidized bed. Lettieri et al.[11] measured pressure drop across a fluidized bed and standard collapse time and compared the fluidization behavior of

FCC catalysts from ambient conditions to 650°C. They found that the increase in temperature affects both hydrodynamic and inter-particle forces and thus causes the fluidization transition from Geldart A to C in the fluidized bed. Shabanian and Chaouki[12] investigated fluidization of coarse particles at high temperature from 700 to 1000°C by pressure measurement, and revealed that the bubbling fluidization of coarse particles at high temperature is principally impacted by the varying gas density if the cohesive inter-particle forces are negligible. They also pointed out that the change in physical and/or physico-chemical properties of fluidized particles and gas due to an increase in temperature should be considered. In addition to pressure measurement, Cui et al.[13] used an optical fiber probe to measure the local void fraction and average void fraction of dense phase to investigate fluidization transition from Geldart A to B for FCC particles in a range of 25-420°C. They showed that the increase in temperature can cause fluidization transition from Geldart A to B, which they attributed to the enhanced inter-particle attractive force and reduced inter-particle repulsive force. However, both pressure transducers and optical fiber probe provide indirect measurement and cannot visualize flow regime transition.

Visualization of fluidized beds at high temperature is critical for studying fluidization transition, especially for the onset of bubbles in a fluidized bed, as the minimum bubbling fluidization is widely accepted as the point, at which the first visual bubble appears. Raso et al. designed a two-dimensional (2D) fluidization facility in an electrically heated refractory furnace,[14] and applied a video camera to record the fluidization processes, up to 900°C. They confirmed the looser stable structure in the fluidized bed even at zero gas velocity induced by enhanced inter-particle forces at high temperature.[14] Later, Formisani et al. further explored the origin of the increase in the void fraction of a packed bed with temperature, and argued that it is clearly related to a variation in inter-particle forces with temperature and classical correlation can be directly used if the dependence of void fraction on temperature is correctly accounted for.[15]However, these results were obtained by visualization of 2D fluidized beds, and may differ from the fluidization occurred in three-dimensional (3D) fluidized beds, where it is difficult to obtain optical images. Recently, Chirone et al. used an X-ray imaging system together with pressure measurement to study the effect of temperature up to 500°C on the minimum fluidization velocity of different Geldart powders (B, A and C) in a 3D fluidized bed of 140 mm in diameter.[16] The X-ray images can capture flow structure, such as gas channels.[16] However, the low temporal resolution and high cost of X-ray imaging system hinder its application in industry.

Electrical capacitance tomography (ECT) is based on capacitance measurement, and is a visualization technique widely used to measure the hydrodynamics of 3D fluidized beds, in particular, solids concentration and distribution, bubble size and bubble rise velocity.[17-20] However, ECT has been mainly used at ambient temperature because of the challenges in making high-temperature ECT sensors and in dealing with the effect of temperature on capacitance measurements and hence image reconstruction. In 2015, we successfully developed high-temperature ECT sensors, which can withstand up to 1000°C,[21-22] and showed that the high-temperature ECT can work well with fluidized beds up to 800°C.[23]Recently, Wang et al. extended the application of high-temperature ECT to measure a slugging fluidized bed of Geldart D powder up to 650°C.[24]

This paper describes first time high-temperature ECT applied to study fluidization of silica particles with mean diameter of 222 μm and density of 2650 kg/m^3, which is typically Geldart B powder under ambient condition. It is shown that high-temperature ECT can visualize the onset of bubbles and fluidization transition of silica particles from Geldart B to A at elevated temperature. Analysis shows that the results agree well with previous studies in literature and the transition is due to enhanced cohesive inter-particle forces induced by high temperature.

Experimental set-up

Figure 1 shows the experimental set-up, i.e. a fluidized bed equipped with a high-temperature ECT sensor, which can work up to 800°C.[23] The fluidized bed is made by a quartz tube of 48 mm inner diameter and 2 mm thick wall. Dried and filtered air is controlled by a mass flowmeter with the range of 0˜30 L/min, and supplied to the fluidized bed through a porous plate gas a distributor of 1 mm thick. Silica particles were

used in experiments, which were first calcined at 600°C for four hours to stabilize the physical and chemical properties. The Sauter mean diameter of silica particles is 222 μm, which was measured using a particle size analyzer (Mastersizer 3000, Malvern Instruments Ltd., UK). Figure 2 shows the size distribution and typical scanning electron microscope image (SEM) of silica particles. The circularity of silica particles is 0.6144 which is measured by analyzing the SEM images. The sphericity of silica particles is replaced by circularity following Kanada.[25] The physical properties and elementary compositions were measured by a Philips Magix-601 X-ray fluorescence spectroscopy (XRF) (see Table 1).

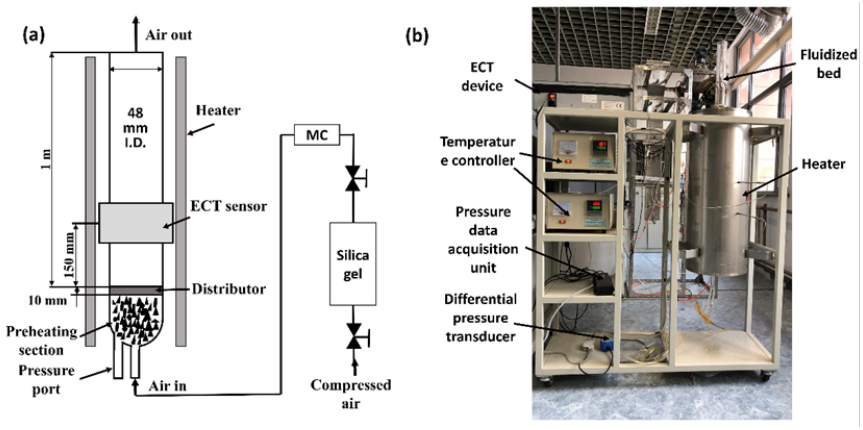

Schematic diagram (b) Photo of experimental facility

Figure 1. Experimental facility, including a fluidized bed equipped with a high-temperature ECT sensor.

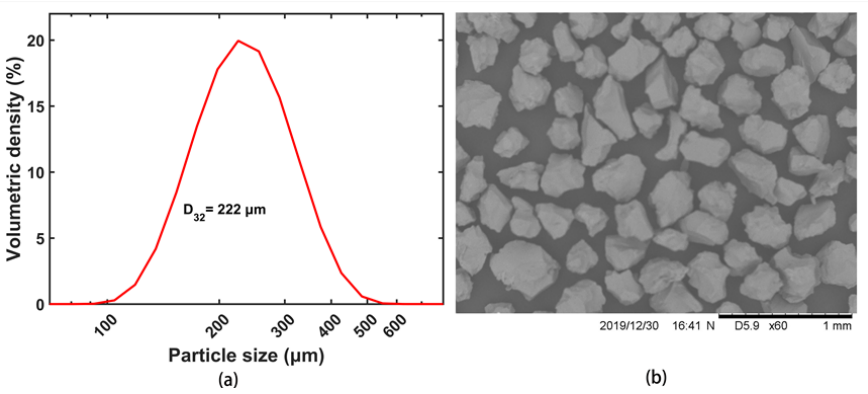

Particle size distribution (b) SEM images of silica particles

Figure 2. Particle size distribution and SEM images.

Table 1. Physical properties and chemical compositions of silica particles.

The total pressure drop across the fluidized bed$P_{\text{total, }V}$, as shown in Figure 1, includes pressure drop of both preheating section and distributor, which was measured by a differential pressure transducer through the pressure port pointing downward. Each time the pressure drop data were recorded continuously at a

sampling rate of 125 Hz and for a duration of 80 seconds. Before an experiment, dried and filtered air was first supplied to the empty bed. By changing the flow rate, the pressure drop across the empty bed was obtained at various superficial gas velocities. Then, for a given superficial gas velocity, the pressure drop was derived by subtracting the pressure drop across the empty bed from the total pressure drop across the bed:

$$P_{\text{fluidized bed, } V} = P_{\text{total, } V} - P_{\text{empty, } V} \quad (1)$$

The high-temperature ECT sensor consists of 8 electrodes. The center of the ECT sensor is located at a horizontal plane, 185 mm above the distributor. The main parameters of the ECT sensor are given in Table 2. It can work up to 800°C. The detailed design was reported in our previous publication.[23]

Table 2. Parameters of high-temperature ECT sensor

Parameters	Value
Column inner diameter	48 mm
Column thickness	2 mm
Number of electrodes	8
Electrode thickness	0.5 mm
Electrode-to-gap ratio	4
Electrode length	30 mm

Experiments were conducted with the same amount of silica particles (i.e. 570 g) at four different temperature settings: 20, 200, 400 and 600°C. For different temperature the gas volumetric flow rate was adjusted based on the ideal gas equation to ensure that superficial gas velocity was increased with the same interval (0.1 cm/s) from the non-fluidized packed bed to slugging bed. In each experiment, empty bed was first heated to the set temperature, and pressure drop across the empty bed at different superficial gas velocity was measured. The ECT sensor was then calibrated for empty fluidized bed as low calibration. Silica particles were loaded into the bed and air was supplied to fluidize the particles. After the bed temperature became stable, air supply was gradually turned off to ensure a stable packed bed. After the packed bed had been stable for 3 minutes, then high calibration was conducted.

Methodology

3.1 Image reconstruction algorithm

For an 8-electrode ECT sensor, in total 28 pairs of inter-electrode capacitance can be obtained and used to reconstruct the relative permittivity distribution.[26] The relation between the capacitance vector and the normalized permittivity vector can be described by

$$\lambda = Sg, \quad (2)$$

where λ is the normalized capacitance vector with the dimension of 28×1 for an 8-electrode sensor, g is the normalized permittivity vector with the dimension of 3228×1 in a circular region,[27] and S is the normalized sensitivity distribution matrix with the dimension of 28×3228.

The linear back-projection algorithm (LBP) and the projected Landweber iteration algorithm with an optimal step length are commonly used to obtain the relative permittivity distribution,[26, 28]

$$\hat{g_0} = S^T\lambda, \quad (3)$$

$$\hat{g_{k+1}} = P\left[\hat{g_k} - \alpha S^T\left(S\hat{g_k} - \lambda\right)\right], \quad (4)$$

$$P[x] = \{$$

$$\begin{array}{lll} 0 & \text{if} & x < 0 \\ x & \text{if} & 0 \le x \le 1 \\ 1 & \text{if} & x > 1 \end{array}, (5)$$

where

$$e^{(k)} = \lambda - S\hat{g}_k \quad (6)$$

$$\alpha = \frac{\left\| S^T e^{(k)} \right\|^2}{\left\| \mathrm{SS}^T e^{(k)} \right\|^2}. \quad (7)$$

Note that $\hat{g}_0$ is derived from the LBP algorithm, which is also regarded as the initial estimation for the projected Landweber iteration algorithm. In Eq. (6), e is the vector of errors between the measured and calculated capacitance vectors. The optimal step length α is computed by Eq. (7) according to Liu et al.[28]. P is the function operator defined in Eq. (5). The number of iterations is set to 200 according to our previous work.[27] The LBP algorithm is used for online visualization and the projected Landweber iteration algorithm with an optimal step length for results comparison considering their characteristics.[26, 28] The effect of temperature on image reconstruction can be referred to our previous work.[23]

Measurement of fluidization characteristics

Once the normalized permittivity distribution ($\hat{g}$) is obtained, the solids concentration distribution and time average solids concentration with its standard deviation can be calculated by the following equations.

$$p = \frac{\sum_{i=1}^{N} \hat{g}_i * s_i}{\sum_{i=1}^{N} s_i} (8)$$

$$p = \frac{1}{Q} \sum_{i=1}^{Q} p_i \ (9)$$

$$\beta = \theta \bullet p \quad (10)$$

$$\beta = \frac{1}{Q} \sum_{i=1}^{Q} \beta_i (11)$$

$$\mathrm{STD} = \frac{1}{Q} \sum_{i=1}^{Q} \left((\beta_i - \beta)^2 \right. (12)$$

where p is the normalized permittivity of each frame; s is the area of each image pixel; N is the number of pixels (3228 in this work); P is the time average normalized permittivity; Q is the number of frames (20000 in this work); $p_i$is the normalized permittivity of i_t frame; β is the solids concentration of each frame, β is the time average solids concentration; β_i is the solids concentration of i_t frame; and STD is the standard deviation ofβ.

Note that θ is solids concentration of the packed bed, which varies with temperature because the packed bed height can expand with the increase in temperature. A parallel model is adopted to construct the relation between the normalized permittivity and the solids concentration as shown in Eq. (10).[18, 29]

Previous studies have shown that packed bed height increases with the increase in inter-particle forces.[14, 15, 34-36] It should be noted that the estimation of solids concentration from ECT images is closely related to the initial packed bed expansion[19, 31, 33, 35] because of the decrease in coordination number of each particle (details can refer the previous study[34]). A specially designed ruler was used to measure the packed bed height. The ruler was made by a stainless-steel rod and held by a device mounted on the outlet of the fluidized bed. It can move freely along the axial direction of the fluidized bed. The packed bed height was recorded according to the surface, below which particles are clearly adhered to the rod.

Results and discussion

4.1 Visualization of fluidization transition

A series of measurements of fluidization at different temperature (T = 20, 200, 400, and 600°C) were carried out using high-temperature ECT. For each temperature, the superficial gas velocity was increased from 0 to 10.0 cm/s with the stepwise increment of 0.1 cm/s. Before measurements for each temperature were made, the static height of the packed bed without gas flow was obtained. The average packed bed height was 22.4, 23.2, 24.4, and 25.7 cm for T = 20, 200, 400, and 600°C, respectively. The corresponding average solids concentrations are listed in Table 3.

Table 3. Average packed bed height and solids concentration at different temperature

Temperature (°C)	Average packed bed height (cm)	Average solids concentration	Average void fraction
20	22.4	0.53	0.47
200	23.2	0.51	0.49
400	24.4	0.49	0.51
600	25.7	0.46	0.54

Figure 3 shows the solids concentration distribution measured by high-temperature ECT. The images of solids concentration distribution were obtained by the projected Landweber iteration algorithm with an optimal step length. As shown in Figure 3, when the superficial gas velocity increases gradually, the occurrence of bubbles can be clearly distinguished, i.e. the transition to bubbling fluidization at different temperature can be identified. A careful check with the snapshots of solids concentration distribution at different temperature suggests that the appearance of first bubble occurs at superficial gas velocity of 3.6, 3.4, 3.2 and 2.9 cm/s for T= 20, 200, 400, and 600°C, respectively.

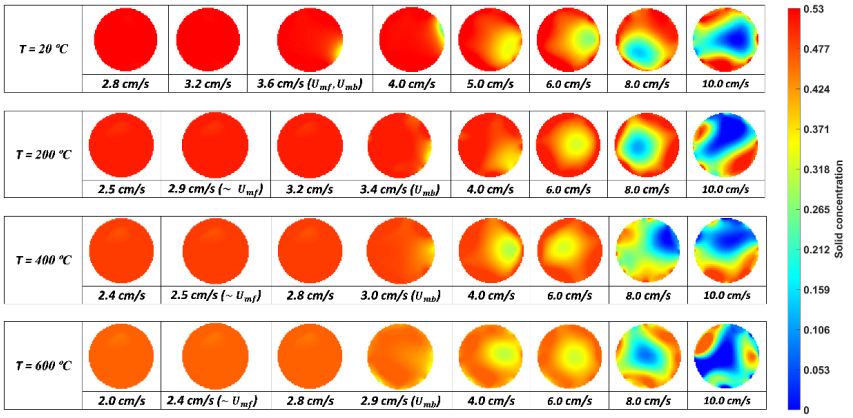

Figure 3. Snapshots of solids concentration distribution at different temperature.

4.2 Minimum bubbling velocity (U_{mb})

It is widely accepted that the minimum bubbling velocity (U_{mb}) is regarded as the superficial gas velocity when bubbles first occur[8, 37-39]. This definition is apparently vague and general, because it largely depends on the methods of visualization. For instance, video camera is normally used to obtain images in 2D fluidized beds. The first occurrence of bubbles in a 2D fluidized bed would be different from that in a 3D fluidized bed with comparable dimension. As shown above, we can distinguish the occurrence of first bubble in 3D fluidized bed via ECT images. However, it would be more precise to quantify U_{mb} by plotting the standard

deviation of average solids concentration of the bed as the function of superficial gas velocity.[28, 40] Figure 4 shows the standard deviation of average solids concentration versus the superficial gas velocity. As can be seen, there exists an apparent jump of standard deviation for each temperature. We found that the superficial gas velocity corresponding to the jump agrees well with our observation on the appearance of first bubble in the fluidized bed. In this sense, we can determine that U_{mb} = 3.6, 3.4, 3.0, and 2.9 cm/s for temperature T= 20, 200, 400, and 600°C, respectively.

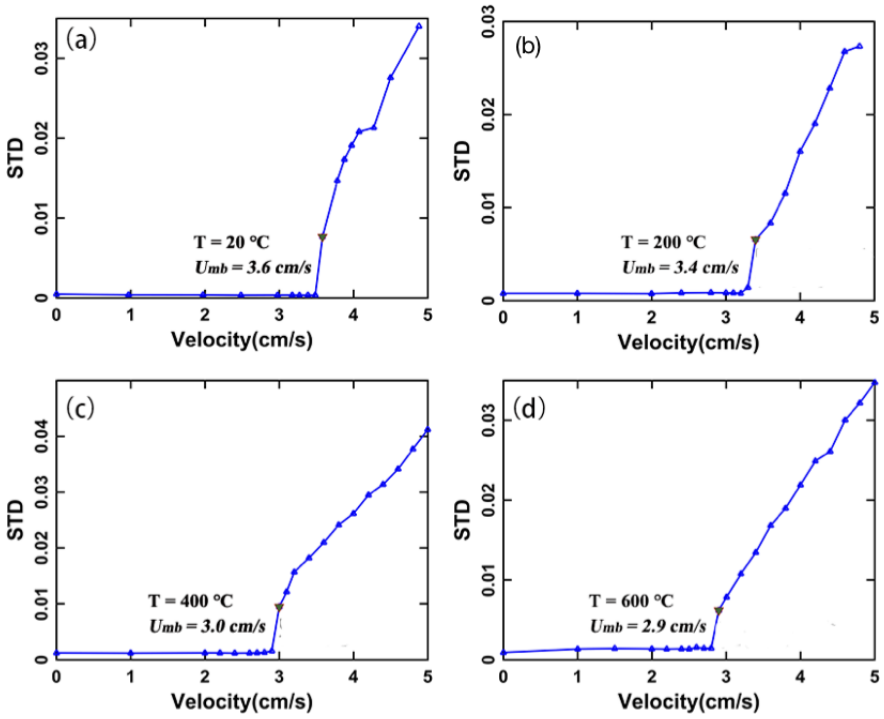

Figure 4. Standard deviation of average solids concentration versus superficial gas velocity at temperature: (a) T = 20 °C, (b) T = 200 °C, (c) T = 400 °C, and (d) T = 600 °C.

In fact, the pressure-drop versus superficial gas velocity curves can also be used to determine U_{mb} according to Rapagnà et al.[42], in which U_{mb} is the point where a shallow minimum occurs, as shown in Figure 5. The minimum bubbling velocity U_{mb} obtained from the pressure-drop versus superficial gas velocity curves is 3.6 cm/s for T =20°C, 3.4 cm/s for T = 200°C, 3.0 cm/s for T = 400°C, and 2.9 cm/s for T = 600°C. This again verified the reliability of high-temperature ECT in measuring the minimum bubbling point in fluidized beds. In conclusion, high-temperature ECT can provide a direct and accurate approach to detecting the minimum bubbling velocity from the reconstructed images of solids concentration of a fluidized bed.

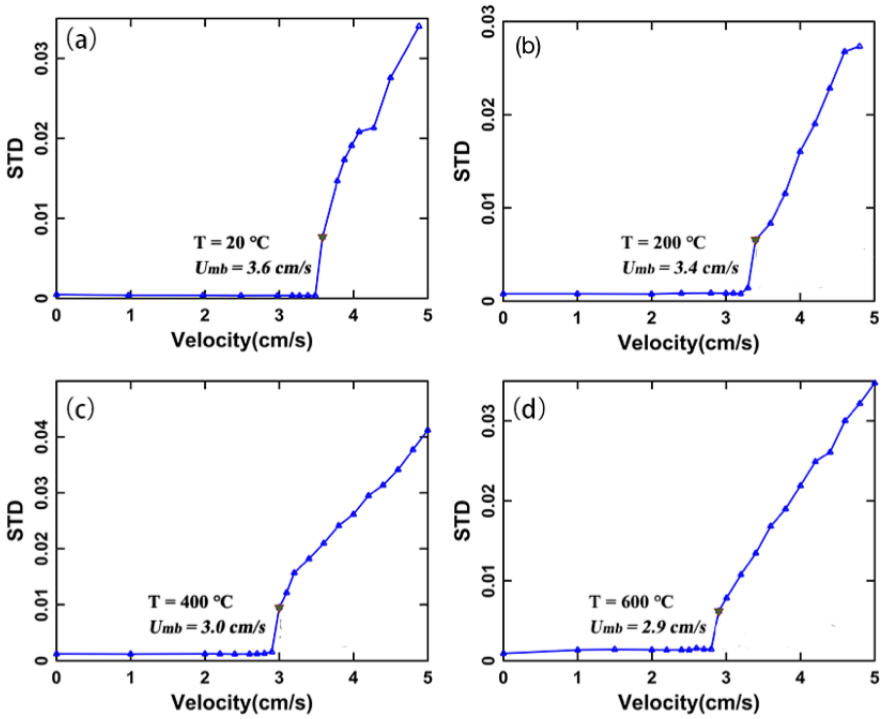

Figure 5. Pressure drop across the fluidized bed versus superficial gas velocity at (a) T = 20°C, (b) T = 200°C, (c) T = 400°C, and (d) T = 600°C.

4.3 Minimum fluidization velocity (U_{mf})

Under ambient conditions, silica particles used in our experiments are typically Geldart B particles. Therefore, the minimum bubbling velocityU_{mb} should be the same as the minimum fluidization velocity (U_{mf}). To determine U_{mf}, we followed pressure drops across the fluidized bed versus superficial gas velocity as shown in Figure 5. It is normally accepted that the point, where the intersection of extrapolated line of pressure drop across the packed bed and that of the total pressure drop across the full fluidized bed, as can be seen in Figure 5, is regarded as the minimum fluidization point.[41] Based on the pressure-drop versus superficial gas velocity curves, we could obtain U_{mf} = 3.60, 2.92, 2.48, and 2.40 cm/s for T= 20, 200, 400, and 600°C, respectively. Apparently, under the ambient condition (T= 20 °C), $U_{mf}$and U_{mb} are coincided.

U_{mf} is compared with the empirical correlations, showing that the dimensionless Ergun equation can be used to predictU_{mf} for Geldart B particles with reasonably good agreement even at high temperature[41]:

$$\frac{1.75}{\varnothing\varepsilon_{mf}^3}\mathrm{Re}_{mf}^2 + 150\frac{1-\varepsilon_{mf}}{\varnothing^2\varepsilon_{mf}^3}\mathrm{Re}_{mf} = Ar \quad (13)$$

where the Reynolds number and Archimedes number are respectively defined as

$$\mathrm{Re}_{mf} = \frac{d_p\rho_g U_{mf}}{\mu} \quad (14)$$

$$Ar = \frac{d_p^3\rho_g(\rho_p-\rho_g)g}{\mu^2} \quad (15)$$

Note that $\varnothing$ is the sphericity of particles,ε_{mf} is the void fraction at minimum fluidization, ρ_p is the particle density, ρ_g is the gas density, d_p is the Sauter mean diameter of particles, $\mu$is the gas viscosity, and g is the gravitational constant.

Figure 6 compares the measured U_{mf} with the predictedU_{mf} via Eq. (13). As can be seen, at relatively low operating temperature (T= 20 and 200°C), the measuredU_{mf} agrees well with the predicted U_{mf}. At

relatively high temperatures, however, the pronounced deviation between the measured and predicted U_{mf} can be observed. Note that in Eq. (13) the effects of gas density and viscosity are taken into account, which implicitly reflects the influence of high temperature via the change in gas properties. It can be argued that at relatively low temperature, the influence of temperature on fluidization of silica particles is mainly exerted via the change in gas properties. At even higher temperature (T = 400 and 600°C), other impact factors, such as enhanced cohesive inter-particle forces, may play an increasingly important role.

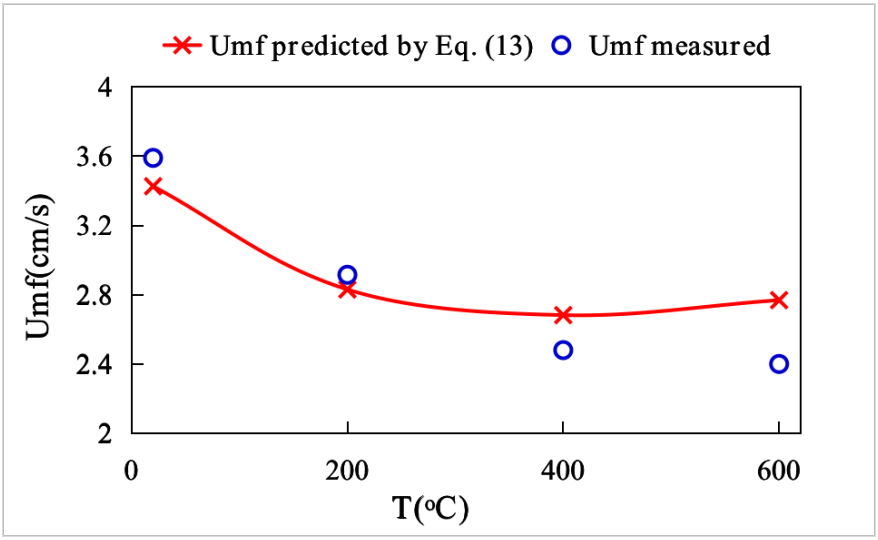

Figure 6. Comparison of U_{mf} obtained from measurements and predictions based on Eq. (13) for different temperature.

4.4 Fluidization transition from Geldart B to A

According to Geldart, fluidization of Geldart B and A particles has typical features as[8]:

- Group B: Bubbles occur when the bed of particles starts to be fluidized, which is featured by $U_{\mathrm{mf}}/\ U_{\mathrm{mb}} = 1$.
- Group A: A homogeneous fluidization regime, in which no obvious bubbles appear between U_{mf} and U_{mb}, leading to $U_{\mathrm{mb}}/U_{\mathrm{mf}} > 1$. Based on the above measurement results,$U_{\mathrm{mb}}/U_{\mathrm{mf}}$ is shown in Figure 7. As can be seen, at ambient condition (T= 20°C), silica particles indeed manifest Geldart B fluidization behavior, i.e.$U_{\mathrm{mf}}/\ U_{\mathrm{mb}} = 1$. When the temperature is increased to 200°C, the occurrence of first bubble happens at $1.164U_{\mathrm{mf}}$, i.e. an interval of homogeneous fluidization between $U_{\mathrm{mf}} \sim 1.164U_{\mathrm{mf}}$ was observed. This is typical Geldart A fluidization behavior. Further increase in temperature to 400°C leads to an enlarged interval of homogeneous fluidization between U_{mf} and $1.209U_{\mathrm{mf}}$, which then levels off to $U_{\mathrm{mf}} \sim 1.201U_{\mathrm{mf}}$ at T= 600°C. Thus, it can be obtained that $U_{\mathrm{mb}}/U_{\mathrm{mf}}$increases from 1.00 at 20°C to 1.201 at 600°C, suggesting that the fluidization transits from Geldart B to A when the operating temperature is increased from ambient to 600°C .

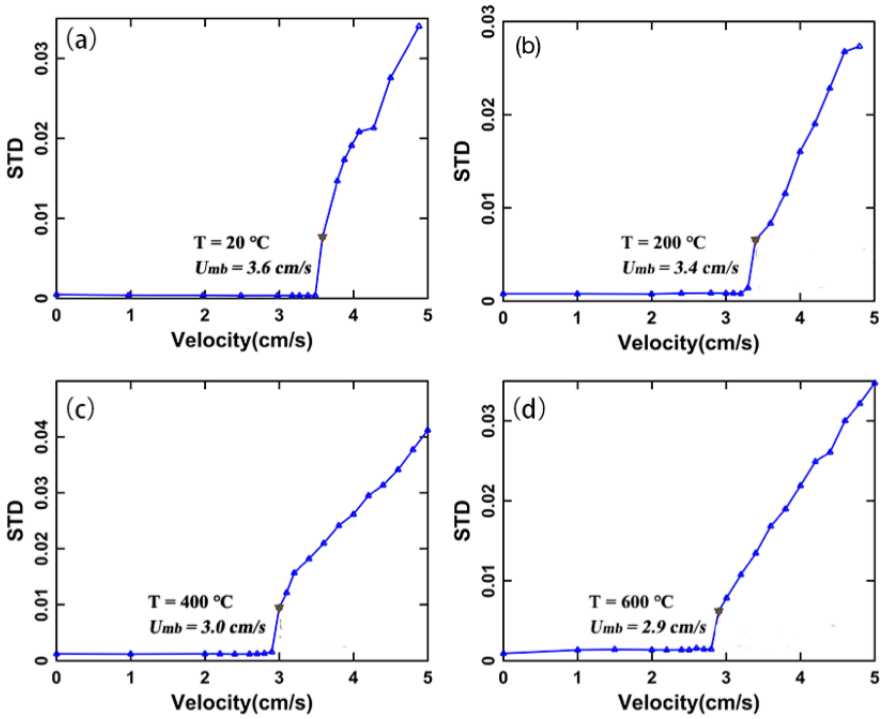

Figure 7. Ratio of $U_{\mathrm{mb}}/U_{\mathrm{mf}}$ at different temperature.

To further understand the mechanism underlying the fluidization transition for silica particles used in this work, we studied the pressure overshoot at the incipient fluidization, which is also shown closely related to the cohesive inter-particle forces.[6, 24-26] Figure 8 shows pressure overshoot, which was obtained by subtracting the local minimum from the maximum of pressure drop over the superficial gas velocity, as shown in Figure 5. The pressure overshoot becomes higher with the increase in temperature, suggesting that the cohesive inter-particle forces are enhanced with the increase in temperature. It was reported that the existence of alkali metal elements in silica particles would cause the change in particle surface property at high temperature, and further increase the cohesive inter-particle forces.[30] From Table 1, it can be seen that the silica particles is mainly composed of Si and O, together with some minor compositions of Al and K. Therefore, the fluidization transition of silica particles from Geldart B to A at elevated temperatures is mainly due to the enhanced cohesive inter-particle forces.

Castellanos et al.[43] found that the pressure overshootP_t can be directly related to the tensile yield strengthσ_t of particles via

$$P_t = \left(\frac{\sigma_t}{\rho_p(1-\varepsilon_{\mathrm{mf}})gH_{\mathrm{mf}}} + 1\right) P_c (16)$$

where H_{mf} is the bed height at the minimum fluidization. The tensile yield strength σ_t can be further used to estimate the cohesive inter-particle forces following Molerus[44]:

$$F_c = \frac{\varepsilon_{\mathrm{mf}}}{1-\varepsilon_{\mathrm{mf}}} d_p^2 \sigma_t (17)$$

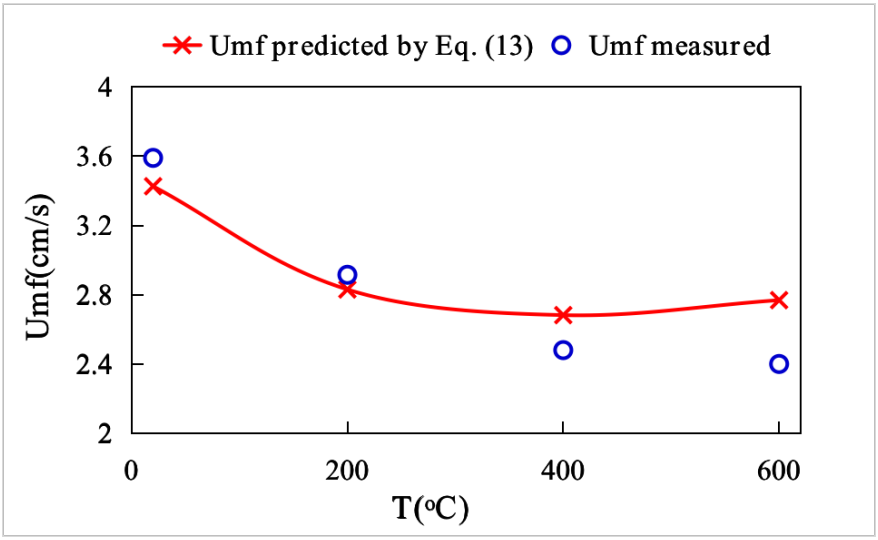

Figure 8. Pressure overshoot of fluidized bed at different temperature.

By Eq. (17) the cohesive inter-particle forces at the incipient fluidization can be estimated. As can be seen in Figure 9(a), the estimated cohesive inter-particle force shows an almost linear increase with the increase in temperature. The Bond number (B_O) that is the ratio of cohesive inter-particle forces to particle weight, can be calculated as $B_O = 0$, 658, 1255, and 1540 for temperature $T = 20$, 200, 400, and 600°C, respectively. Such high Bond number B_O at high temperature may be the reason for the fluidization transition of Geldart B to A for silica particles. Previous studies under ambient conditions show a typical range of B_O less than 1 for several Geldart A powders (e.g. FCC catalyst and Al_2O_3 powders)[45]. However, Valverde and Castellanos[46] showed that for a modified 8.53 μm xerographic toner with B_O of 550, a fluidization transition from Geldart C to A was observed. The hydrodynamic forceF_N can be calculated by[44]

$$F_N = \varepsilon_{\mathrm{mf}} d_p^2 \rho_P g H_{\mathrm{mf}} \quad (18)$$

It can be compared with the cohesive inter-particle force. Figure 9(b) shows that $\frac{F_C}{F_N}$ increases with temperature.$\frac{F_C}{F_N}$ is less than 7% at relatively low temperature (20 and 200°C), but increases to more than 12% at relatively high temperature (400 and 600°C). A level off of $\frac{F_C}{F_N}$ at high temperature can also be identified, which is akin to the variation of$\frac{U_{\mathrm{mb}}}{U_{\mathrm{mf}}}$, indicating that the level off of $\frac{U_{\mathrm{mb}}}{U_{\mathrm{mf}}}$ at T = 400 and 600°C is closely related to that of$\frac{F_C}{F_N}$.

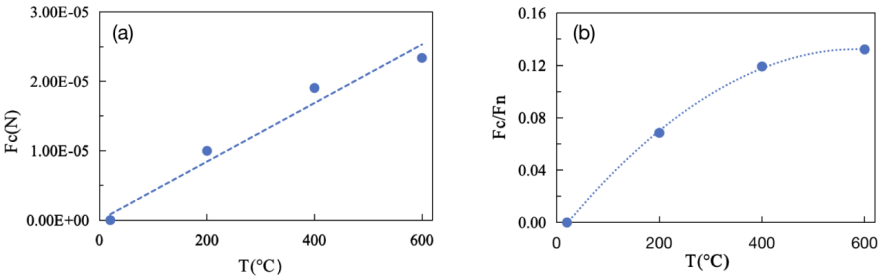

Figure 9. Cohesive inter-particle forces induced by high temperatures: (a) cohesive inter-particle force F_C and (b) ratio$\frac{F_C}{F_N}$.

The elevated temperature may influence the fluidization behavior in a fluidized bed via two aspects. On the

one hand, it may change the gas properties, such as gas density and viscosity, which essentially affect the hydrodynamic interaction between particles and gas. On the other hand, it can alter the surface property of particles and thus cause varying cohesive inter-particle forces. Based on the above discussion, it can be concluded that for the silica particles used in this study, at relatively low temperature the effect of cohesive inter-particle forces plays a minor role, and so the change in gas properties due to elevated temperature is responsible for the fluidization behavior. At relatively high temperature, the change in particle surface properties which causes variation of cohesive inter-particle forces due to the variation in temperature becomes very important. In summary, both aspects make a coupled yet complicated contribution to the fluidization transition from Geldart B to A as observed in this work.

Conclusions

By the use of a recently developed high-temperature ECT, we first time observed that the onset of bubbles in a fluidized bed with silica particles, which typically manifest Geldart B fluidization at ambient temperature, but shift to a lower superficial gas velocity at a higher operation temperature. Further analysis of standard deviation of solids concentration derived from ECT images, as well as the pressure drop profile, suggests that $U_{\mathrm{mb}}/U_{\mathrm{mf}}$ increases from 1.0 to around 1.2 as the increase in temperature from 20 to 600°C. This indicates that there exists fluidization transition from Geldart B to A induced by high temperature for silica particles studied in this work and the visualization of homogeneous fluidization regime by ECT. Our results showed that the elevated temperature influences the fluidization behavior in a fluidized bed via two aspects: (1) changing gas properties, such as gas density and viscosity and (2) altering surface property of particles and thus cohesive inter-particle forces. At relatively low temperature the effect of cohesive inter-particle forces plays a minor role, and so the change in gas properties due to increase in temperature is responsible for the fluidization behavior. At relatively high temperature, the enhanced cohesive inter-particle forces because the change in particle surface properties becomes much more important. Both aspects make a coupled yet complicated contribution to the fluidization transition from Geldart B to A for silica particles. These results agree well with previous studies in the literature. The advantages of using high-temperature ECT to investigate the fluidization behavior include high temporal resolution, robust, reliable, and low cost. Therefore, high-temperature ECT is promising and is expected to open up a new approach to in-situ measurement of 3D fluidized beds under real industrial operation conditions.

Acknowledgments

We are grateful to the National Key Research and Development Program of China (Grant No. 2018YFB0604904), the National Natural Science Foundation of China (Grant No. 91834302) and the Newton Advanced Fellowship of the Royal Society, UK (Grant No. NA140308).

NOMENCLATURE:

P:pressure drop

S: normalized sensitivity matrix

G: normalized permittivity distribution

N: Number of pixels in measurement zone, 3228 in this study

e: Error vector

P: Function operator

p: Normalized permittivity

s: Pixel area

Q: Number of frames of each measurement, 20,000 in this study

STD: Standard deviation of average solids concentration

??? : Minimum bubbling velocity, cm/s

??f : Minimum fluidization velocity, cm/s

Re_{mf} : Reynolds number at incipient fluidization

$\varnothing$: Sphericity

d_p: Sauter diameter of silica

Ar: Archimedes number

P_t: Pressure overshoot

P_c: Fluidized bed pressure drop

H_{mf}: Bed height at incipient fluidization

F_c: Cohesive inter-particle forces

F_N: Hydrodynamic force

Greek symbols

g: Normalized capacitance vector

?: Optimal step length

β: Solids concentration

θ: Solids concentration of a packed bed

ε_{mf} : Void fraction at incipient fluidization

ρ_g: Air density

μ : Gas viscosity

ρ_p: Silica density

σ_t: Tensile yield strength

Superscript

-: Average value

References

1. Alamolhoda, F.; Shamiri, A.; Hussain, M. A.; Zarghami, R.; Sotudeh-Gharebagh, R.; Mostoufi, N., Detection of Agglomeration by Analysis of Vibration Signatures in a Pilot-Scale fluidized Bed Reactor of Propylene Polymerization, Int. J. of Chem. Reactor Eng., 2019, 17, 2.
2. Chmelar, J.; Matuska, P.; Gregor, T.; Bobak, M.; Fantinel, F.; Kosek, J., Softening of polyethylene powders at reactor conditions, Chem. Eng. J., 2013, 228, 907-916.
3. Datta, S.; Sarkar, P.; Chavan, P. D.; Saha, S.; Sahu, G.; Sinha, A. K.; Saxena, V. K., Agglomeration behaviour of high ash Indian coals in fluidized bed gasification pilot plant, Applied Thermal Eng., 2015, 86, 222-228.
4. Elled, A. L.; Amand, L. E.; Steenari, B. M., Composition of agglomerates in fluidized bed reactors for thermochemical conversion of biomass and waste fuels, Fuel 2013, 111, 696-708.

5. Montes, A.; Ghiasi, E.; Tran, H.; Xu, C., Study of bed materials agglomeration in a heated bubbling fluidized bed (BFB) using silica sand as the bed material and KOH to simulate molten ash, Powder Technol., 2016, 291, 178-185.
6. Zhong, Y.; Wang, Z.; Guo, Z.; Tang, Q., Prevention of agglomeration/defluidization in fluidized bed reduction of Fe2O3 by CO: The role of magnesium and calcium oxide, Powder Technol., 2013, 241, 142-148.
7. Ye M.; Li H.; Zhao Y.; Zhang T.; Liu Z., MTO process development: The key of mesoscale studies, Advances in Chem. Eng., 2016, 47: 279-335
8. Geldart, D., Types of gas fluidization, Powder Technol., 1973, 7, 285-292.
9. Botterill, J. S. M., Teoman, Y. and Yuregir, K. R., The effect of operating temperature on the velocity of minimum fluidization, bed voidage and general behaviour, Powder Technol., 1982, 31, 101-110.
10. Lucas, A., Arnaldos, J., Casal, J. and Puigjaner, L., High temperature incipient fluidization in mono and polydisperse systems, Chem. Eng. Comm., 1986, 41, 121-132.
11. Lettieri, P.; Newton, D.; Yates, J. G., High temperature effects on the dense phase properties of gas fluidized beds, Powder Technol., 2001, 120, 34-40.
12. Cui, H.; Chaouki, J., Inter-particle forces in high temperature fluidization of Geldart A particles, China Particuology, 2004, 2, 113-118.
13. Shabanian, J.; Chaouki, J., fluidization characteristics of a bubbling gas–solid fluidized bed at high temperature in the presence of inter-particle forces, Chem. Eng. J., 2016, 288, 344-358
14. Raso, G.; Damore, M.; Formisani, B.; Lignola, P. G., The Influence of Temperature on the Properties of the Particulate Phase at Incipient fluidization, Powder Technol., 1992, 72, 71-76.
15. Formisani, B.; Girimonte, R.; Mancuso, L., Analysis of the fluidization process of particle beds at high temperature, Chem. Eng. Sci., 1998, 53, 951-961.
16. Chirone R.; Poletto M.; Barletta D.; Lettieri, P., The effect of temperature on the minimum fluidization conditions of industrial cohesive particles, Powder Technol., 2020, 362, 307–322.
17. Makkawi, Y. T.; Wright, P. C., fluidization regimes in a conventional fluidized bed characterized by means of electrical capacitance tomography, Chem. Eng. Sci., 2002, 57, 2411-2437.
18. Du, B.; Warsito, W.; Fan, L.-S., ECT studies of the choking phenomenon in a gas-solid circulating fluidized bed, AIChE J., 2004, 50, 1386-1406.
19. Li, X.; Jaworski, A. J.; Mao, X., Bubble size and bubble rise velocity estimation by means of electrical capacitance tomography within gas-solids fluidized beds, Measurement, 2018, 117, 226-240.
20. Guo, Q.; Meng, S.; Zhao Y.; Ma, L.; Wang D.; Ye M.; Yang W.; Liu, Z., Experimental verification of solid-like and fluid-like states in the homogeneous fluidization regime of Geldart A particles, Ind. Eng. Chem. Res., 2018, 57, 2670-2686.
21. Ye M.; Luo Q.; Meng S.; Zhang T.; and Liu Z., An electrical capacitance tomography sensor withstanding high temperature and its fabrication method, Chinese Patent: ZL201510623768.9, 25 Sept. 2015.
22. Ye M.; Guo Q.; Meng S.; Zhang T.; and Liu Z., An electrical capacitance tomography sensor withstanding high temperature, Chinese Patent: ZL201510967356.7, 18 Dec. 2015.
23. Huang, K.; Meng, S.; Guo, Q.; Ye, M.; Shen, J.; Zhang, T.; Yang, W.; Liu, Z., High-temperature electrical capacitance tomography for gas–solid fluidized beds, Meas. Sci. Technol., 2018, 29, 104002.
24. Wang, D.; Xu, M.; Marashdeh, Q.; Straiton, B.; Tong, A.; Fan, L.-S., Electrical Capacitance Volume Tomography for Characterization of Gas–Solid Slugging fluidization with Geldart Group D Particles under High Temperatures, Ind. Eng. Chem. Res., 2018, 57, 2687-2697.
25. Kanada T., Estimation of sphericity by means of statistical processing for roundness of spherical parts, Precision Eng., 1997, 20, 117-122
26. Yang, W. Q.; Peng, L., Image reconstruction algorithms for electrical capacitance tomography, Meas. Sci. Technol., 2003, 14 (1), R1-R13
27. Liu, S.; Fu, L.; Yang, W. Q., Optimization of an iterative image reconstruction algorithm for electrical capacitance tomography, Meas. Sci. Technol., 1999, 10 (7), L37-L39.
28. Huang, K.; Meng, S.; Guo, Q.; Yang, W.; Zhang, T.; Ye, M.; Liu, Z., Effect of Electrode Length of

an Electrical Capacitance Tomography Sensor on Gas-Solid fluidized Bed Measurements, Ind. Eng. Chem. Res., 2019, 58 (47), 21827-21841.
29. Banaei, M.; van Sint Annaland, M.; Kuipers, J. A. M.; Deen, N. G., On the accuracy of Landweber and Tikhonov reconstruction techniques in gas-solid fluidized bed applications, AIChE J., 2015, 61 (12), 4102-4113.
30. Grace, J. R.; Sun, G., Influence of particle size distribution on the performance of fluidized bed reactors, The Canadian J. of Chem. Eng., 1991, 69 (5), 1126-1134.
31. Agrawal, V.; Shinde, Y. H.; Shah, M. T.; Utikar, R. P.; Pareek, V. K.; Joshi, J. B., Estimation of Bubble Properties in Bubbling fluidized Bed Using ECVT Measurements, Ind. Eng. Chem. Res., 2018, 57 (24), 8319-8333.
32. Chandrasekera, T. C.; Li, Y.; Moody, D.; Schnellmann, M. A.; Dennis, J. S.; Holland, D. J., Measurement of bubble sizes in fluidized beds using electrical capacitance tomography, Chem. Eng. Sci., 2015, 126, 679-687.
33. Agu, C. E.; Pfeifer, C.; Eikeland, M.; Tokheim, L.-A.; Moldestad, B. M. E., Models for Predicting Average Bubble Diameter and Volumetric Bubble Flux in Deep fluidized Beds, Ind. Eng. Chem. Res., 2018, 57 (7), 2658-2669.
34. Shabanian, J.; Chaouki, J., Hydrodynamics of a gas–solid fluidized bed with thermally induced interparticle forces, Chem. Eng. J., 2015, 259, 135-152.
35. Chandrasekera, T. C.; Li, Y.; Moody, D.; Schnellmann, M. A.; Dennis, J. S.; Holland, D. J., Measurement of bubble sizes in fluidized beds using electrical capacitance tomography, Chem. Eng. Sci., 2015, 126, 679-687.
36. Xu, C.; Zhu, J. X., Effects of gas type and temperature on fine particle fluidization, China Particuology, 2006, 4 (3-4), 114-121.
37. Rhodes, M. J.; Wang, X. S.; Forsyth, A. J.; Gan, K. S.; Phadtajaphan, S., Use of a magnetic fluidized bed in studying Geldart Group B to A transition, Chem. Eng. Sci., 2001, 56 (18), 5429-5436.
38. Ye, M.; van der Hoef, M. A.; Kuipers, J. A. M., A numerical study of fluidization behavior of Geldart A particles using discrete particle model, Powder Technol., 2004, 139: 129-139.
39. Ye, M.; van der Hoef, M. A.; Kuipers, J. A. M., The effects of particle and gas properties on the fluidization of Geldart A particles, Chem. Eng. Sci., 2005, 60 (16), 4567-4580.
40. Agu, C. E.; Tokheim, L.-A.; Eikeland, M.; Moldestad, B. M. E., Determination of onset of bubbling and slugging in a fluidized bed using a dual-plane electrical capacitance tomography system, Chem. Eng. J., 2017, 328, 997-1008.
41. Subramani, H. J.; Mothivel Balaiyya, M. B.; Miranda, L. R., Minimum fluidization velocity at elevated temperatures for Geldart's group-B powders, Experimental Thermal and Fluid Science, 2007, 32 (1), 166-173
42. Rapagna, S.; Foscolo, P.U.; Gibilaro, L.G. , The influence of temperature on the quality of gas fluidization, Int. J. Multiph. Flow, 1994, 20, 305-313.
43. Castellanos A.; Valverde, J.M. ; Quintanilla, M.A.S., The Sevilla powder tester: a tool for characterizing the physical properties of fine cohesive powders at very small consolidations, KONA Powder Part J. 2004, 22 , 66–81
44. Molerus O., Theory of Yield of Cohesive Powders, Powder Technol., 1975, 12, 259-275
45. Guo Q.; Meng S.; Zhao Y.; Ma L.; Wang D.; Ye M.; Yang W.; Liu Z., Experimental verification of solid-like and fluid-like states in the homogeneous fluidization regime of Geldart A particles, Ind. Eng. Chem. Res., 2018, 57, 2670-2686.
46. Valverde, J. M.; Castellanos, A., Types of gas fluidization of cohesive granular materials, Phys. Rev. E, 2007, 75, 031306.
47. Girimonte, R.; Formisani B., The minimum bubbling velocity of fluidized beds operating at high temperature, Powder Technol., 2009, 189, 74-81.